Please cite this article in press as: Bénéfice et al., Dry mass photometry of single bacteria using quantitative wavefront microscopy, Biophysical Journal (2023), https://doi.org/10.1016/j.bpj.2023.06.020

Biophysical Journal
Article

Biophysical Society

Dry mass photometry of single bacteria using quantitative wavefront microscopy

Maëlle Bénéfice,[1] Aurore Gorlas,[2] Baptiste Marthy,[1] Violette Da Cunha,[2] Patrick Forterre,[2,3] Anne Sentenac,[1] Patrick C. Chaumet,[1] and Guillaume Baffou[1,*]

[1]Institut Fresnel, CNRS, Aix Marseille University, Centrale Marseille, Marseille, France; [2]Université Paris-Saclay, CEA, CNRS, Institute for Integrative Biology of the Cell (I2BC), Gif-sur-Yvette, France; and [3]Département de Microbiologie, Institut Pasteur, Paris, France

ABSTRACT Quantitative phase microscopy (QPM) represents a noninvasive alternative to fluorescence microscopy for cell observation with high contrast and for the quantitative measurement of dry mass (DM) and growth rate at the single-cell level. While DM measurements using QPM have been widely conducted on mammalian cells, bacteria have been less investigated, presumably due to the high resolution and high sensitivity required by their smaller size. This article demonstrates the use of cross-grating wavefront microscopy, a high-resolution and high-sensitivity QPM, for accurate DM measurement and monitoring of single microorganisms (bacteria and archaea). The article covers strategies for overcoming light diffraction and sample focusing, and introduces the concepts of normalized optical volume and optical polarizability (OP) to gain additional information beyond DM. The algorithms for DM, optical volume, and OP measurements are illustrated through two case studies: monitoring DM evolution in a microscale colony-forming unit as a function of temperature, and using OP as a potential species-specific signature.

SIGNIFICANCE Quantitative phase microscopy techniques are capable of measuring the dry mass of biological cells in culture using optical microscopy means, usually for eukaryotic cells in the hundred-picogram range. This study provides the guidelines for accurately measuring dry masses in the subpicogram range, for the study of microorganisms, such as bacteria or archaea, opening the path for the precise monitoring of bacteria growth at the single-cell level. Moreover, this study extends the possibilities of quantitative phase microscopies by introducing new measurable quantities besides dry mass, such as complex optical polarizability and normalized optical volume, with envisioned applications in cell classification using deep learning.

INTRODUCTION

Mass density and refractive index of transparent materials are closely related. This trend is far from being a universal law for *organic* and *inorganic* materials, as stressed in 1954 by Barr, who objectively compared a wide range of materials (1). For *biological* matter, however, it is widely recognized that an increase in mass density results in a corresponding increase in the refractive index, especially when the system of interest is mainly composed of proteins (2–4). The law holds true for living cells, for instance, where the mass density ρ and the refractive index n of the cell are linked by the relation

$$n - n_{\text{water}} = \gamma(\rho - \rho_{\text{water}}), \tag{1}$$

where γ, called the specific refraction increment, is roughly constant, varying within the tight range 0.18–0.21 μm^3 pg^{-1} (we chose $\gamma = 0.20$ μm^3 pg^{-1} in this article). ρ_{water} and n_{water} are the mass density and refractive index of water. Water is taken as the reference liquid because cells are normally living and cultured in aqueous environment.

Based on this relation, Barer initiated in 1954 the idea of using phase imaging to measure the dry mass (DM) of cells (2). Indeed, quantitative phase microscopy (QPM) techniques map the phase shift ϕ, or equivalently the optical path difference (OPD) $\delta\ell = \phi\lambda/2\pi$, associated with a transparent object of interest in the field of view of a microscope, typically biological media such as living cells. The measured OPD image reads

$$\delta\ell(x,y) = \int (n(x,y,z) - n_{\text{water}})\text{d}z. \tag{2}$$

Submitted February 24, 2023, and accepted for publication June 26, 2023.

*Correspondence: guillaume.baffou@fresnel.fr

Editor: Alberto Diaspro.

https://doi.org/10.1016/j.bpj.2023.06.020

Please cite this article in press as: Bénéfice et al., Dry mass photometry of single bacteria using quantitative wavefront microscopy, Biophysical Journal (2023), https://doi.org/10.1016/j.bpj.2023.06.020

The integral runs over the thickness of the imaged object. The so-called optical volume (OV) δV is defined as the integral of the OPD over the area of interest

$$\delta V = \iint \delta\ell(x,y)\mathrm{d}x\mathrm{d}y = \iiint (n(x,y,z) - n_{\mathrm{water}})\mathrm{d}x\mathrm{d}y\mathrm{d}z \quad (3)$$

and can be simply retrieved from OPD images by a pixel summation. From Eqs. 1 and 3, one can derive the important equation linking the measured OPD ($\delta\ell$) or phase (ϕ) image with the DM δm of the imaged object:

$$\delta m = \gamma^{-1} \iint \delta\ell(x,y)\mathrm{d}x\mathrm{d}y, \quad (4)$$

$$\delta m = \gamma^{-1}\frac{\lambda}{2\pi} \iint \phi(x,y)\mathrm{d}x\mathrm{d}y. \quad (5)$$

The DM is considered as a faithful estimation of the biomass of the system, more than the fresh mass that does not exclude water, and especially in cell biology. Imaging also enables the mapping of the DM surface density $\delta\sigma$, in pg $\mu\mathrm{m}^{-2}$:

$$\delta\sigma(x,y) = \gamma^{-1}\delta\ell(x,y). \quad (6)$$

This relation directly leads to the simple relation between OV and DM:

$$\delta m = \gamma^{-1}\delta V.$$

Here are the relations to be used in practice, including the common units:

$$\delta\sigma(x,y)\ \left[\mathrm{pg}/\mu\mathrm{m}^2\right] = 5.0 \times 10^{-3}\ \delta\ell(x,y)\ [\mathrm{nm}].$$

$$\delta m\ [\mathrm{pg}] = 5.0\ \delta V\ \left[\mu\mathrm{m}^3\right].$$

Although the idea of measuring biomass using QPM was introduced in 1954, its implementation remained elusive for 50 years (5,6). One had to wait for the development of high-resolution QPM techniques in the 2000s to observe the publication of the first influential articles on this topic. In 2008, Popescu et al. illustrated the principle of DM measurement of living cells using QPM in a seminal article by measuring the DM of HeLa cells (7). The authors could measure cell biomasses of a few hundred picograms using two QPM techniques, namely Fourier phase microscopy and Hilbert phase microscopy. The group reported a sensitivity of 4 fg $\mu\mathrm{m}^{-2}$. Simultaneously, Marquet's group reported measurements of the DM production rate of yeast cells using digital holography microscopy (8). DMs of wild-type and mutant cells of a few tens of picograms were measured and followed through the cell cycle. In 2011, another seminal article was published by the group of Popescu using, this time, spatial light interference microscopy and focusing on *Escherichia coli* (9). DMs of a few picograms were measured, demonstrating the ability of QPM to answer the important question of whether cell growth is linear or exponential. In 2012, Girshovitz and Shaked introduced the wide variety of mass-OPD-related physical quantities that can be measured by QPM, besides DM and DM surface density, namely the OV, the cell outer surface, some phase/mass ratiometric quantities, sphericity/eccentricity indices, and some statistical parameters (phase kurtosis and skewness) (10). The interest of all these quantities was illustrated by using HeLa cells.

Quadriwave lateral shearing interferometry (QLSI) is a high-resolution optical wavefront imaging technique (11). QLSI is simply based on the use of a two-dimensional diffraction grating (also known as cross-grating) placed at a millimetric distance from the sensor of a camera (12). When a QLSI camera is implemented on a microscope, it can then be referred to as cross-grating wavefront microscopy (CGM) (13,14). In 2015, Aknoun et al. introduced the use of CGM for the measurements of DM of mammalian cells (15). The interest of directly measuring $\delta\ell$ and not ϕ to access cellular DM was illustrated, and a detailed study on the precision and trueness of the DM measurements was conducted. The authors also addressed an important aspect of DM measurements, i.e., cell segmentation, by detailing an effective segmentation algorithm for eukaryotic cells, even in confluence.

All these phase and wavefront microscopy techniques were then used to tackle biological questions related to cell growth and proliferation (16–28). Measuring DM is certainly the main strength of QPM compared with more common microscopy approaches based on fluorescence measurements. QPM lacks specificity but is quantitative, noninvasive and can run for days without inducing photobleaching or phototoxicity to the sample. All these articles also illustrate the interest of accessing cellular DM using optical microscopy compared with microelectromechanical techniques (20,29–32). Surprisingly, measuring DM by a phase or wavefront microscopy technique has remained elusive for microorganisms such as bacteria until very recently (33,34), and the microbiology community would gain a lot if there was a simple tool to quantitatively monitor the growth rate of microorganisms under a microscope, and not only within an incubator.

In this article, we use CGM to demonstrate its ability to simply and accurately measure the DM of small cells, such as bacteria. We explain how to handle diffraction fringes, inherent to micrometric objects, to avoid possible inaccuracies in the DM estimation. We also quantify the accuracy of the measured DM as a function of microscope focus and objective numerical aperture. Then, we introduce the use of the optical polarizability (OP), measured by CGM, as a complementary information to DM. Finally, the method is illustrated on two case studies: the monitoring of the DM evolution of a microscale colony-forming unit (CFU) and

Please cite this article in press as: Bénéfice et al., Dry mass photometry of single bacteria using quantitative wavefront microscopy, Biophysical Journal (2023), https://doi.org/10.1016/j.bpj.2023.06.020

its dependence on temperature, and the use of the OP as a ratiometric measurement to help classify imaged bacteria.

MATERIALS AND METHODS

Image acquisition using CGM

QLSI, introduced and patented by Primot and Guerineau in 2000 (12,35), is based on the use of a two-dimensional grating (or the synonym, cross-grating) positioned at a millimetric distance from a camera chip (13). A QLSI cross-grating consists of a $0 - \pi$ phase checkerboard pattern that favors the diffraction of only the first orders. The measured interferogram enables the computation of both the intensity and wavefront profiles of a light beam, with higher accuracy and definition compared with Shack-Hartman wavefront sensors. When QLSI is implemented on a microscope (11), a configuration we recently proposed to name CGM for the sake of simplicity, the measured intensity and wavefront profiles become the transmittance and the OPD of the imaged object, as demonstrated by Bon et al. in 2009 for applications in biology (36). More recently, applications in nanophotonics have been reported by our group to image and characterize nano-objects (37–40).

The $0 - \pi$ phase shift pattern is key to obtain a nondiffractive light wave between the grating and the camera, meaning that the light wave propagates keeping the same pattern. This shadow-like propagation creates an array of dots on the camera, the position of which can be precisely determined if they are sampled, in practice, by at least 3 camera pixels. As a consequence, the definition of the QLSI image is reduced by a factor of 3, in the two dimensions of the image, leading to the reduction by a factor of 9 of the total amount of pixels.

All the experiments were conducted on a home-made microscope (Fig. 1) composed of a monochromator as a light source (Monochromator associated with an Energetiq EQ-99X laser-driven light source, purchased from Opton Laser International, Les Ulis, France, hyperchromator DG-600-300/1250) mounted in a Köhler configuration. The monochromator was tuned at a wavelength $\lambda = 540$ nm or $\lambda = 625$ nm depending on the experiments. We used Olympus objective lenses (100× [oil, 1.3 NA] UPLFLN100XOP/100× [oil, variable NA] UPLFLN100XOI2/40× [air, 0.6 NA] LUCPLFN40X/60× [oil, 1.25 NA] UPLFLN60XOI); a tube lens with a focal length of 200 mm (Thorlabs, Maisons-Laffitte, France, TTL200-A), multiplying the effective magnification of the microscope by a factor of 1.1, compared with the objectives; a QLSI wavefront imaging system, consisting of a Zyla camera 5.5 and a QLSI cross-grating of pitch $\Gamma = 39$ μm placed at 0.86 mm from the camera sensor.

Sample preparation

E. coli and *Geobacillus stearothermophilus* were usually cultivated in LB medium overnight at 37°C, 200 rpm. *Lactobacillus reuteri* was precultured in MRS medium overnight at 35°C, 200 rpm. *Deinococcus radiodurans* was precultured in TGY2X medium overnight at 30°C, 200 rpm. The archaeon *Sulfolobus shibatae* was cultivated in 182 medium over 3 days at 75°C, 200 rpm. The bacterial and archaeal concentrations were evaluated by measuring the optical density (OD) of the culture (Ultrospec 10 Cell Density Meter, Biochrom, Cambridge, United Kingdom).

Different sample geometries were used depending on the experiment.

For the experiments on the effect of the focus and the numerical aperture: a volume of 5 μL of bacteria with an OD of 0.4 was sandwiched between two glass coverslips (Ø25 mm at the bottom and Ø18 mm at the top) and placed in a metallic sample holder (Attofluor Cell Chamber, Thermo Fisher Scientific, Illkirch, France). After 15 min of sedimentation, the bacteria were imaged using the microscope.

For the experiments related to precision estimation: a volume of 10 μL of bacteria suspension with an optical density of 0.05 was left to dry on a microdish with a glass bottom and 400 μL of LB culture media was added on top. A Ø25-mm glass coverslip was added on top of the medium, to ensure a stable, flat upper interface, not likely to distort the incoming light wavefront. Then, the bacteria were imaged after 30 min of sedimentation.

For the experiments on *E. coli* growth as a function of the temperature, see cell heating below.

Cell heating

For any experiment at higher temperature than the ambient temperature, the bacteria were heated using a microheating device (VAHEAT, Interherence, Erlangen, Germany), consisting of a sample holder of the size of a glass slide that contains a glass coverslip in which an electrical current can flow. The heating coming from the glass coverslip directly enables a fast temperature control over a square area of around 5×5 mm^2 at the bacteria location. This small heating device enables a simple and fast control of the temperature (around 1 s to reach the temperature target and a few seconds to cool down to room temperature). The experiments were conducted on two types of samples, the Standard Smart Substrates (SmS) and the Standard Smart Substrates with PDMS reservoir (SmS-R). With SmS, a volume of

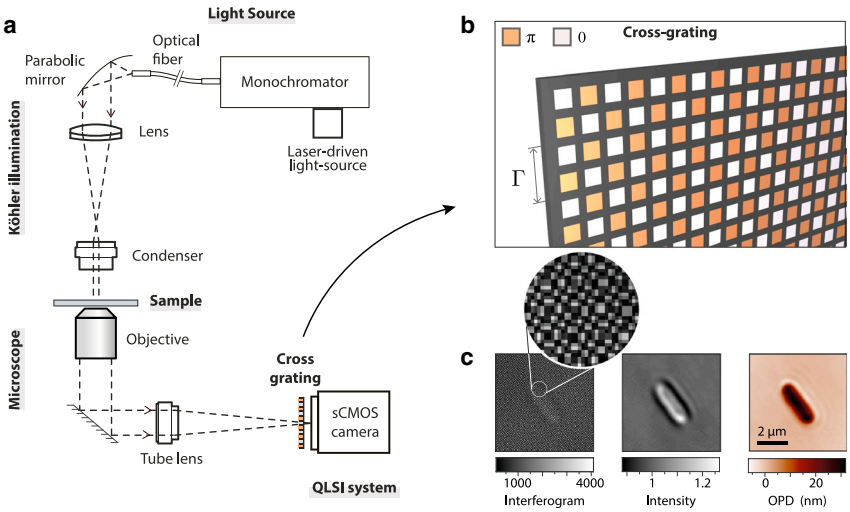

FIGURE 1 Experimental setup for cross-grating wavefront microscopy. (*a*) Schematic of the microscope. (*b*) Schematic of the 2D-grating (also known as cross-grating) placed at a distance of 0.86 mm from the camera sensor. (*c*) From left to right, raw camera image called the interferogram, transmittance image, and OPD image, both retrieved from the interferogram. To see this figure in color, go online.

Please cite this article in press as: Bénéfice et al., Dry mass photometry of single bacteria using quantitative wavefront microscopy, Biophysical Journal (2023), https://doi.org/10.1016/j.bpj.2023.06.020

0.5 μL of bacteria suspension with an OD of 0.05 was deposited on the substrate and covered by the 5×5 mm^2 coverslip to prevent convection. For the SmS-R, the PDMS cuvette was filled with LB culture medium, and an extra 25-mm glass coverslip was added on top of the cuvette to prevent evaporation during the experiment and ensure a flat, stable top interface.

Numerical simulations

IF-DDA is a free software that we developed to rigorously solve the problem of electromagnetic scattering of small objects in three dimensions (41). The software can be downloaded from the webpage https://www.fresnel.fr/perso/chaumet/ifdda.html. IF-DDA is based on the discrete dipole approximation (DDA), which is a volume-integral equation method (42). The principle consists of discretizing the object under study in three dimensions on a cubic mesh, computing the electromagnetic field inside the object, and computing the subsequent light emission by the object through a microscope to get the electromagnetic field at the object plane.

RESULTS AND DISCUSSION

DM δm measurement method

Eqs. 3 and 4 introduced the calculation method of the OV and DM of an object from its OPD image. In practice, the double integration amounts to summing pixel values over a domain $\mathcal{D}$ of the image:

$$\delta V = p^2 \sum_{i,j \in \mathcal{D}} \delta \ell_{i,j}, \tag{7}$$

$$\delta m = \gamma^{-1} p^2 \sum_{i,j \in \mathcal{D}} \delta \ell_{i,j}, \tag{8}$$

where p^2 is the pixel area. Provided a good background subtraction is performed, the domain of integration $\mathcal{D}$ is easy to define when considering eukaryotic cells (15). However, it is a priori less obvious to determine when dealing with small objects because of diffraction, which makes the boundaries of the object not well defined. We recently pointed out this issue with the DM measurement of neurites using CGM (43). Fig. 2 *a* displays a simulated OPD image of a bacterium, of the rod-shape of an *E. coli*, obtained using IF-DDA (see materials and methods). One can see that diffraction rings spread much further than the geometrical size of the bacteria, raising the question of what the proper integration area $\mathcal{D}$ should be to properly calculate the DM δm and OV δV using Eqs. 7 and 8. To numerically answer this question, we calculated the OV of an *E. coli* bacterium as a function of the size of the integration area $\mathcal{D}$ (Fig. 2 *b*), and compared with the theoretical value $\delta V = (n - n_0)V$. We define a dilation factor $f = d/d_0$, where d_0 is the width of the bacteria and d is the width of the domain $\mathcal{D}(f)$. The plot of Fig. 2 *b* shows that integrating over $\mathcal{D}(f = 1)$, i.e., over the geometrical size of the bacteria, or over what a segmentation algorithm would normally capture, tends to yield inaccurate measurements. Around $f = 1$, the values are slightly underestimated (0.0122 instead of the true value of 0.0131 μm^3), and the slope of $\mathcal{D}(f)$ remains large, making any OV and DM measurement likely to feature a large dispersion of the measurements. Fig. 2 *b* also shows that, if the diffraction rings are all captured within the integration area $\mathcal{D}(f)$, the measured DM and OV tend toward the theoretical values (0.0131 μm^3 and 65 fg, respectively). Thus, for a proper estimation of DM and OV, the diffraction rings must be all captured.

Experimentally, because these diffraction rings are tenuous, standard segmentation algorithms tend to miss them. For this reason, we recently proposed a refined algorithm aimed to capture them in the context of neuron imaging (43). The algorithm we developed in MATLAB (The MathWorks, Natick, MA) and provide on GitHub (44) is depicted in Fig. 3. It involves a first step of segmentation of the cell, which can be performed using any regular segmentation algorithm. We chose a magic wand approach where, by clicking on a bacterial cell, the whole body of the bacterium is automatically selected. Then, the selected domain $\mathcal{D}$ is resized by a factor f and the OV, calculated over the domain $\mathcal{D}(f)$, is plotted as a function of f. This plot naturally

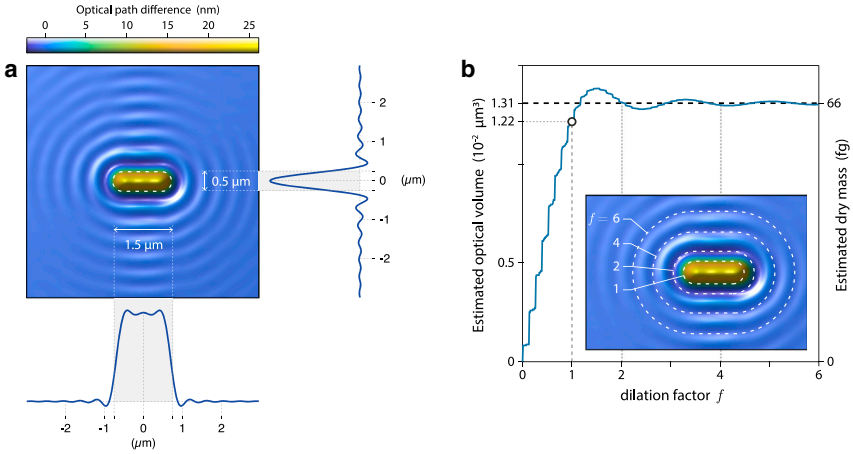

FIGURE 2 IF-DDA numerical simulation of the image of a bacterium, at focus, on glass in water, modeled as a rod of length 1.5 μm, diameter 0.5 μm, and refractive index 1.38 ($\lambda = 550$ nm, 1.3 NA). (*a*) Simulated OPD image of the bacterium along with horizontal and vertical crosscuts passing by the center of the bacterium. The dashed line represents the geometry of the bacteria. (*b*) Estimated OV and DM as a function of the dilation factor f of the area over which the image integration is numerically performed. The dashed line represents the theoretical values. The dashed lines in the inset represent the geometries of several integration areas $\mathcal{D}(f)$ for various dilation factors f (1, 2, 4, and 6). To see this figure in color, go online.

Please cite this article in press as: Bénéfice et al., Dry mass photometry of single bacteria using quantitative wavefront microscopy, Biophysical Journal (2023), https://doi.org/10.1016/j.bpj.2023.06.020

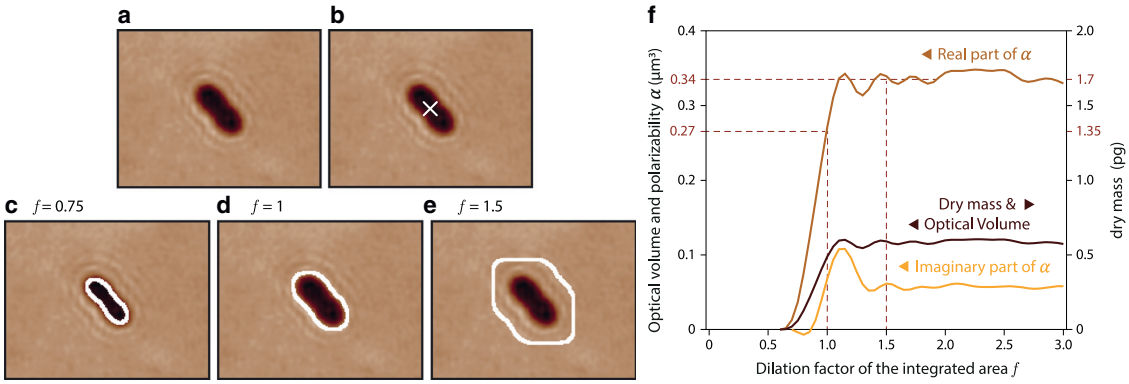

FIGURE 3 Procedure of segmentation for DM estimation. (*a*) Experimental OPD image of a bacterium. (*b*) Magic-wand selection. (*c–e*) Segmented areas for various dilation factors f: 0.75, 1 (that the standard segmentation gives), and 1.5 (the minimum segmented area to consider for proper DM estimation). The background value is calculated over the white, annular area that is 3 px wide. (*f*) Estimated OV, OP, and DM as a function of the dilation factor f. To see this figure in color, go online.

shows an increase in OV as a function of f from $f = 0$ to $f = 1$ until it reaches a plateau corresponding to a proper capture of the diffraction rings and to the true OV. The plateau is reached at an f value of around 1.5, substantially greater than 1, demonstrating the need to capture a larger area than a regular segmentation algorithm would. Above $f = 1$, oscillations of the estimated DM are observed due to the diffraction rings, which are barely visible but substantially affect the DM estimation.

Caution should be used, though, with experimental OPD images. Unlike simulated images, which naturally exhibit a zero OPD value far from the imaged objects, experimental OPD images are obtained to within an arbitrary additional constant. Indeed, CGM primarily measures *gradients* of OPD, and the OPD image is subsequently obtained by integration of these gradients, which adds an arbitrary constant. To circumvent this specificity of CGM, we neither undertake to adjust the background offset nor correct any background nonuniformity. Instead, for each estimation of the OV or DM at a particular f value, we simply subtract to the image the average OPD value over the boundary of the segmented area $\mathcal{D}(f)$ (represented by the white area in Fig. 3, *c–e*). This method yields a precise and simple estimation of OV and DM, and is not sensitive to the arbitrary offset of the OPD and to any nonuniformity of the OPD background. Fig. 3 *f* plots the measured OV as a function of the dilation factor f using the methods depicted above. Note that image noise can limit the range of f values, as explained further below.

As a conclusion, diffraction rings must be taken into account for an accurate measurement of the DM. Even if they look tenuous, they contribute to a substantial part of the information. This conclusion is consistent with our recent study on nanoparticles (100 nm in size) much smaller than bacteria, which also featured diffraction rings that must be integrated to yield a proper estimation of the optical complex polarizability of the nanoparticle (39). The interest of measuring the OV on a plateau of $\delta V(f)$, rather than at $f = 1$, is not only to obtain a value closer to reality. The other, and equally important, interest of expanding the summation area is that the slope of $\delta V(f)$ is weaker (Fig. 3 *f*), leading to much less dispersed measurements, and thus more reproducible and precise DM estimation.

Optical polarizability α measurements

Besides the OV and DM, we introduce in this article another physical quantity to be measured from the optical images that also contain valuable information: the complex optical polarizability (OP) α (39). We introduced the ability of CGM to measure this quantity in a previous publication dealing with metallic and dielectric nanoparticles (39). The OP α is a complex number that characterizes the optical response of the nanoparticle. Unlike the DM or the OV, which can be calculated from the sole OPD image, the calculation of α involves a mix of both the intensity (i.e., transmittance) and OPD images, T and $\delta\ell$:

$$\alpha = \frac{i\lambda n_0}{\pi}\iint\left(1 - \sqrt{T(x,y)}\exp(i2\pi\delta\ell(x,y)/\lambda)\right)\mathrm{d}x\mathrm{d}y, \tag{9}$$

$$\alpha = \frac{i\lambda n_0 p^2}{\pi}\sum_{i,j\in D}\left(1 - \sqrt{T_{i,j}}\exp\left(i2\pi\delta\ell_{i,j}/\lambda\right)\right), \tag{10}$$

where n_0 is the refractive index of the substrate (usually glass). Compared with δV, α is richer because it also contains information coming from the intensity image. Also, as demonstrated below, α can give ratiometric measurements, no longer dependent on the bacteria size, and representing a signature of the bacteria type.

The OP has the dimension of a volume, just like the OV. There exists an interesting relation between OP and OV. For $\delta\ell \ll \lambda$ (which is normally the case for bacteria), a Taylor

Please cite this article in press as: Bénéfice et al., Dry mass photometry of single bacteria using quantitative wavefront microscopy, Biophysical Journal (2023), https://doi.org/10.1016/j.bpj.2023.06.020

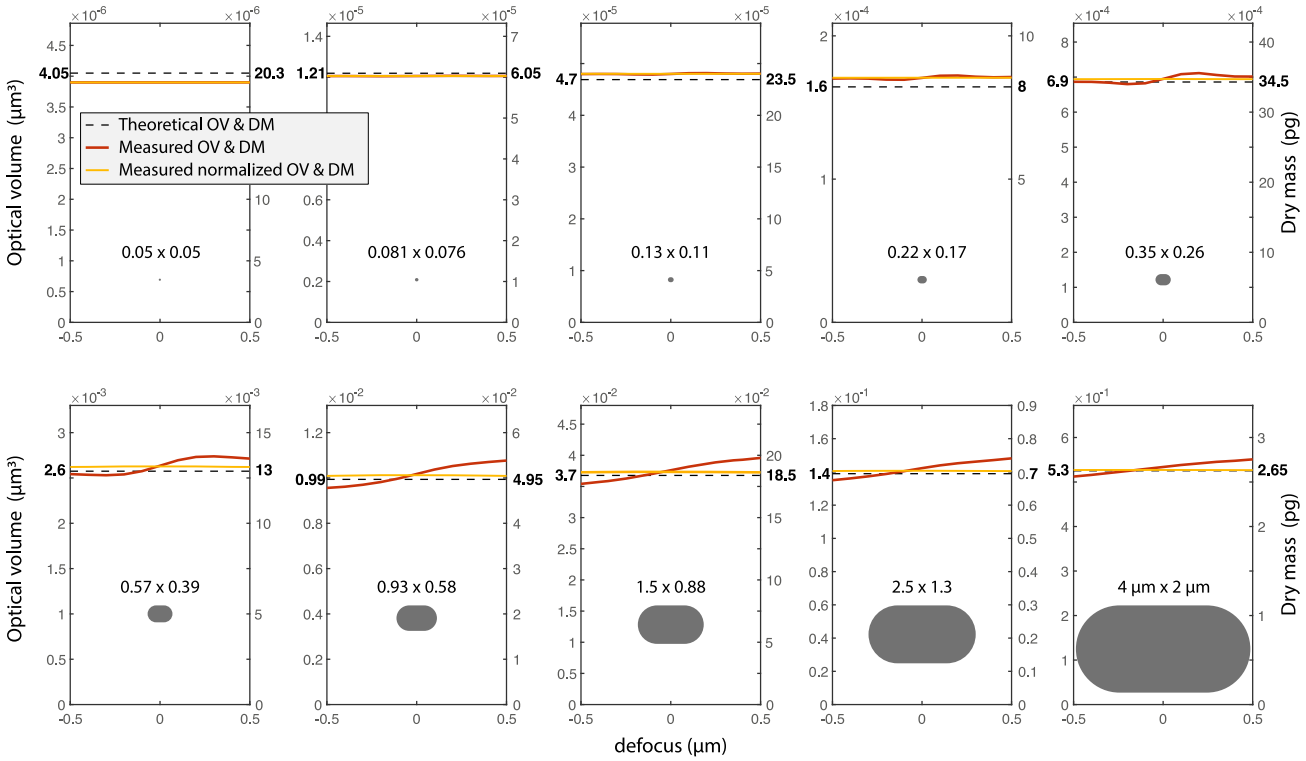

FIGURE 4 OV and DM measured on numerical OPD images of 10 micro-objects, simulated using IF-DDA, as a function of the microscope focus. The morphologies span progressively from a 50-nm sphere to a 4 × 2-μm rod. The objects feature a refractive index of $n = 1.38$, are deposited on glass (1.51), and immersed in water ($n_0 = 1.33$). In each case, a drawing of the object is inserted, specifying the dimensions of the object. The dashed lines represent the theoretical OV and DM. The red (*darker*) lines represent the OV and DM measured on the OPD images by pixel summation according to Eqs. 7 and 8. The yellow lines represent the weighted OV and DM measured on the OPD images by pixel summation according to Eq. 13. To see this figure in color, go online.

development at the first order gives the following expression for the real part of α:

$$\mathrm{Re}(\alpha) \approx -2n_0p^2\sum_{i,j\in D}\sqrt{T_{i,j}}\delta\ell_{i,j}\,. \tag{11}$$

For $T \approx 1$ (a good approximation for transparent objects), from Eq. 11, the real part of the OP and the OV become proportional:

$$\delta V \approx -\mathrm{Re}(\alpha)\,/\,(2n_0)\,. \tag{12}$$

In addition to having the same dimension, the OP and OV have thus the same order of magnitude.

From Eqs. 11 and 12, one can define the weighted OV δV_w, defined from the OPD image weighted by the transmittance image:

$$\delta V_w \approx \sum_{i,j\in D}\sqrt{T_{i,j}}\delta\ell_{i,j}\,. \tag{13}$$

Because δV_w is defined from the OP which tends to be focus independent (39), we shall see in the next section that considering the weighted OV δV_w (Eq. 13) instead of normal δV (Eq. 7) makes the estimation of the OV, and thus the DM, less focus dependent and more precise.

Validity of DM measurements as a function of the object size

Eq. 2, and all the following equations used to determine OV and DM, suppose the projective approximation. This approximation is no longer valid in the case of small particles, where ray optics no longer applies. Nanoparticles can even feature plasmonic or Mie resonances, making the measured OV far from being only dependent on the volume of the object, because surface effects dominate bulk properties. The question of whether DM measurements can be performed on nano-objects is thus relevant. In this section, we conduct DDA simulations to investigate the accuracy of OV measurements as a function of the object size. We chose to consider objects that vary progressively from a 50-nm sphere (corresponding to a virus or a vesicle) to a 4 × 2-μm elongated rod (corresponding to a large bacteria), immersed in water, lying on glass. The refractive index of the objects was kept at 1.38, a typical value for cells. We also varied the focus from −0.5 to 0.5 μm for each object. Results are plotted in Fig. 4. In each simulated OPD image, a pixel summation (Eq. 7) was performed to determine the so-called imaged OV (*red solid lines*). The main observation is that OV and DM measurements can be safely conducted even for the smallest objects. In particular, for small objects, measured and

Please cite this article in press as: Bénéfice et al., Dry mass photometry of single bacteria using quantitative wavefront microscopy, Biophysical Journal (2023), https://doi.org/10.1016/j.bpj.2023.06.020

theoretical OV line shapes are indistinguishable (first three graphs of Fig. 4). There is just a weak dependence of the imaged OV as a function of the focus, in particular for large objects, which makes the OV measurements less accurate when the microscope is defocused. This focus dependence is studied in more detail in the next section. The conclusion here is that DM measurements can be safely conducted for arbitrarily small biological objects.

Here, we stopped the simulation at a minimum size of 50 nm because it would be difficult to image objects smaller than that using any QPM. Note that, using interferometric scattering, (iSCAT), it is possible to detect single proteins and, if a proper calibration is performed, it is even possible to determine their mass (45).

Influence of image noise on the measurements of δm and α

The primary source of noise in CGM is the shot noise (also known as photon noise) (14). Thermal or reading noise can be considered as negligible because the intensity on the camera sensor in CGM is normally high. This shot noise creates a white noise on the interferogram and on the measured wavefront gradients. Upon integrating the wavefront gradients to get the OPD image, this white noise turns into a Brown noise (or Flicker noise) (14). While white noise features a uniform spectral distribution, a Brown noise is characterized by a spectral distribution in $1/F^2$ (the inverse of spatial frequency squared), meaning that low frequencies are particularly important in the noise of OPD images in CGM.

To investigate the effect of this particular noise on DM and OP measurements, we conducted numerical simulations. We simulated flat images endowed with a Brown noise, where we fixed the noise standard deviation at $\sigma_0 = 0.17$ nm, a typical value in CGM. The OV on this image was estimated using Eq. 8, over a circular area of radius R, as defined in Fig. 5 *a*. Of course, the OV is supposed to be zero because no object is imaged (float OPD). This is true in average, but not for each particular image due to noise. Fig. 5 *b* plots the calculated OV as a function of R using the procedure described in Fig. 3. Counterintuitively, although the noise has an averaged value of zero over the image, integrating the noise leads to a divergence of $\delta V(R)$ when increasing R (Fig. 5 *b*). We calculated the standard deviation σ_{OV} of the calculated OV for a large set of noise images (5000 noise images), and found a law scaling as $\sigma_{OV} \sim R^2$ (Fig. 5 *c*). This divergence comes from the fact that the noise is a Brown noise dominated by low spatial frequencies. For a white noise, the divergence would be less dramatic, scaling as R. However, as far as the scaling law is not faster than R^2, the OV of an imaged object also scale as R^2. This means that if the signal of the imaged object is larger than the noise, its DM could be measured no matter the object's size. The same conclusion and scaling law apply for the estimation of α.

Fig. 6 further illustrates the effect of the noise of OPD images on DM and polarizability measurements, with the OV measurement on a single bacterium and with a common size (OV of around 0.2 μm^3). The measured OV and OP are plotted as a function of the integration radius R, both for a bare field of view (Fig. 6 *a*) and with the bacterium (Fig. 6 *b*). From this comparison, one can see that the effect of the noise becomes detrimental from $R \sim 90$ px, much further than the onset of the plateau at $R \sim 50$ px (see Fig. 6 *b*) where the measurements should be done. Thus, for bacteria, and more generally for anything that stands out from the noise, precise OV and OP measurements can be done. Things are more difficult when dealing with nanoparticles, for instance. Gold nanoparticles, 100 nm in diameter, could be precisely characterized, for instance, with normal imaging conditions (averaging of 30 interferograms). For smaller objects, such as vesicles of viruses, for instance, the estimation of the DM could be more difficult, but could always be improved by averaging more interferograms. A detailed description of the noise of OPD images acquired using CGM, and on how to minimize it, is provided in (14).

Dependence of δm and α measurements on focus and numerical aperture

Changing the focus of the microscope strongly affects the intensity and OPD images, from which the OV, DM, and

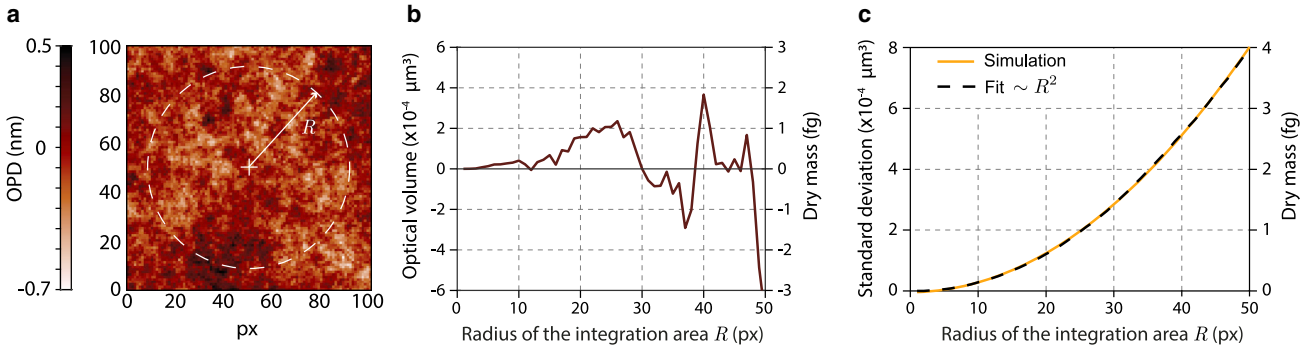

FIGURE 5 Application of the DM estimation algorithm on a noise image. (*a*) Simulated OPD noise image (100 ×100 px). The integration domain $\mathcal{D}$ consists of a disc of radius R. (*b*) OV and DM estimated using Eqs. 7 and 8 over $\mathcal{D}$ as a function of R. (*c*) Standard deviation of the measured OV and DM over 5000 noise images as a function of R, and fit of the profile by the function $R \to aR^2$. To see this figure in color, go online.

Please cite this article in press as: Bénéfice et al., Dry mass photometry of single bacteria using quantitative wavefront microscopy, Biophysical Journal (2023), https://doi.org/10.1016/j.bpj.2023.06.020

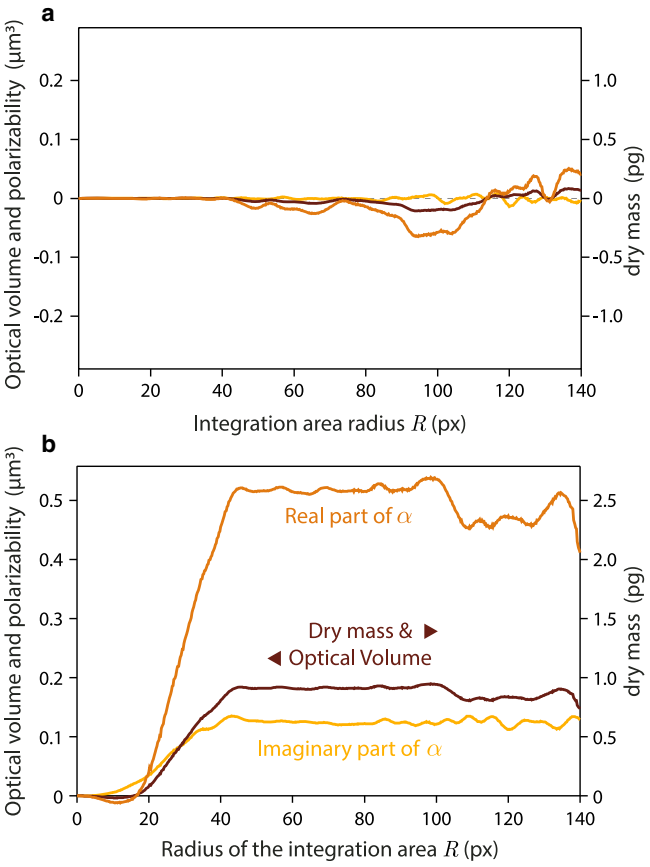

FIGURE 6 OP, OV, and DM as a function of the integration radius, (*a*) without any object on the image (only noise), and (*b*) in the presence of a bacterium. To see this figure in color, go online.

OP are calculated. The imaged objects look more blurred when the microscope is defocused. It is thus important to determine to what extent the focus affects the estimations of these quantities. The focus is indeed not straightforward to determine and can vary from one image to another. When visually adjusting the focus of a microscope, what is perceived as the right focus can be user-dependent and, as a more subtle problem, the right focuses usually look much different when looking at the intensity or OPD images. Because of this uncertainty, it is important to determine the focus range that yields reproducible values of OV, DM, and OP. A similar issue is a priori possible with the numerical aperture (NA) of the microscope, which affects the image in the same manner as the focus.

The case of the dependence of DM on the focus has been studied using CGM with eukaryotic cells by Aknoun et al. (15), who showed that the measured DMs do not vary more than 1% if the defocus remains within ± 5 μm. This weak dependence comes from the fact that refraction and diffraction are negligible for eukaryotic cells. The authors also showed that the NA does not affect the cells' DM measurements at all. Since bacteria are much smaller than eukaryotic cells, and their OPD images more affected by diffraction and more dependent on the focus and the NA, these rules derived for eukaryotic cells should be reconsidered for bacteria.

Regarding the OP α, we demonstrated in a previous publication that its estimation is supposed to be rigorously independent on the focus and NA if the surrounding medium is uniform (39). However, cells in culture lie at the vicinity of a glass/water interface, making the surroundings nonuniform. The OP α is thus no longer supposed to remain constant in theory.

To quantify the effect of the focus and NA on the estimation of OV, DM, and OP of objects as small as bacteria, we conducted numerical and experimental studies, presented below.

Fig. 4 displays numerical simulations of the OV of nano- and micro-objects as a function of the focus of the microscope, from -0.5 to 0.5 μm. These simulations demonstrate a slight dependence of OV on the focus, especially for large objects (not for nanoparticles). However, OV variations remain confined within 10% maximum if the focus is varied by ± 0.5 μm. This range of variation does not preclude OV measurements. Interestingly, using the normalized OV defined by Eq. 13 enables the cancellation of this dependence, for any size of the imaged object, and the estimation of the proper OV. The use of the intensity-normalized OV thus appears as an effective way to limit the dispersion of OV measurements. Note that these simulations do not specifically concern CGM. These results apply for any QPI.

To investigate the effect of the focus, we also conducted experiments on *E. coli* bacteria. Bacteria cultures were imaged at room temperature, not at the optimal growth temperature of 37°C. This way, the bacteria did not grow over the duration of the experiment to ensure that variations of the measured DMs from one image to another do not come from actual DM variations.

The focus was varied from -7 to $+7$ μm. This wide range of values is purposely exaggerated as a means to better cover the subject. In practice, for bacteria, the focus can be visually set within a range of ± 1 μm with a good reproducibility (see Fig. 7 *a*). Fig. 7, *b–d* demonstrate a substantial effect of the focus on the measured OV and α values. Unlike eukaryotic cells that demonstrate a parabolic dependence of the measured δm values as a function of the focus (15), we found a linear dependence for bacteria. However, substantial deviation of δm and α are only observed for defocuses that can be easily avoided experimentally. Within the more reasonable range of ± 1.5 μm, both the OP and OV can be considered constant. Caution should therefore be taken when measuring these optical parameters, the focus should remain in the -1.5, 1.5 μm range to ensure accurate values of the OV, DM, and OP.

We also conducted a similar study to analyze the influence of the objective NA on the DM δm and OP α measurements. Fig. 8 displays the normalized OV and the

Please cite this article in press as: Bénéfice et al., Dry mass photometry of single bacteria using quantitative wavefront microscopy, Biophysical Journal (2023), https://doi.org/10.1016/j.bpj.2023.06.020

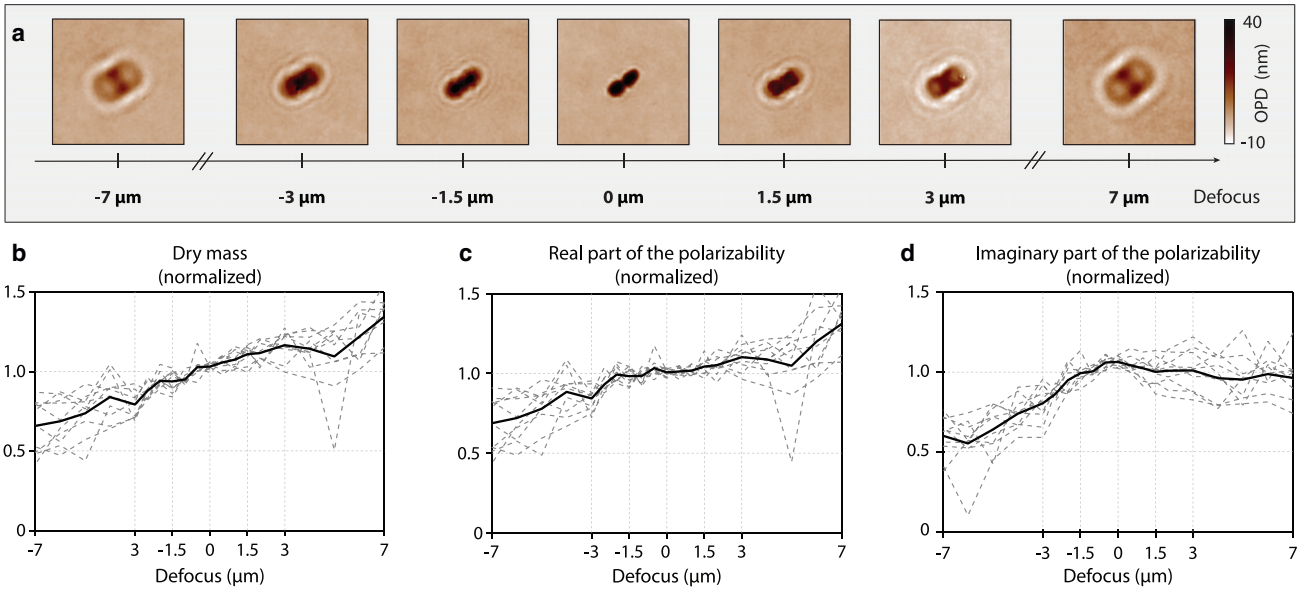

FIGURE 7 Dependence of DM and OP on focus. (*a*) OPD images of a single bacterium for different image focuses (100×, 1.3 NA, $\lambda = 540$ nm). (*b*) Normalized DM as a function of the defocus for 10 different bacteria (*dashed lines*), along with the average of all these line shapes (*solid line*). (*c*) Same as (*b*) for Re(α). (*d*) Same as (*c*) for the Im(α). In (*b–d*), all the line shapes have been normalized by the average value over the range ± 2 µm. To see this figure in color, go online.

normalized real and imaginary parts of the OP as a function of the objective NA from 0.6 to 1.3. The NA of the objective has no influence on the measurement of the OV and OP. No caution need to be taken regarding the objective NA when conducting DM measurements using CGM. The same conclusion was reported for the DM of eukaryotic cells (15) and for the OP of nanoparticles (39).

Precision of the measurements

To estimate the precision of OV and DM measurements on bacteria, we acquired a series of 60 successive images on a given set of 10 bacterial cells, and measured the OV of all these cells on all these images using the algorithm depicted in Fig. 3. One frame was acquired (no image

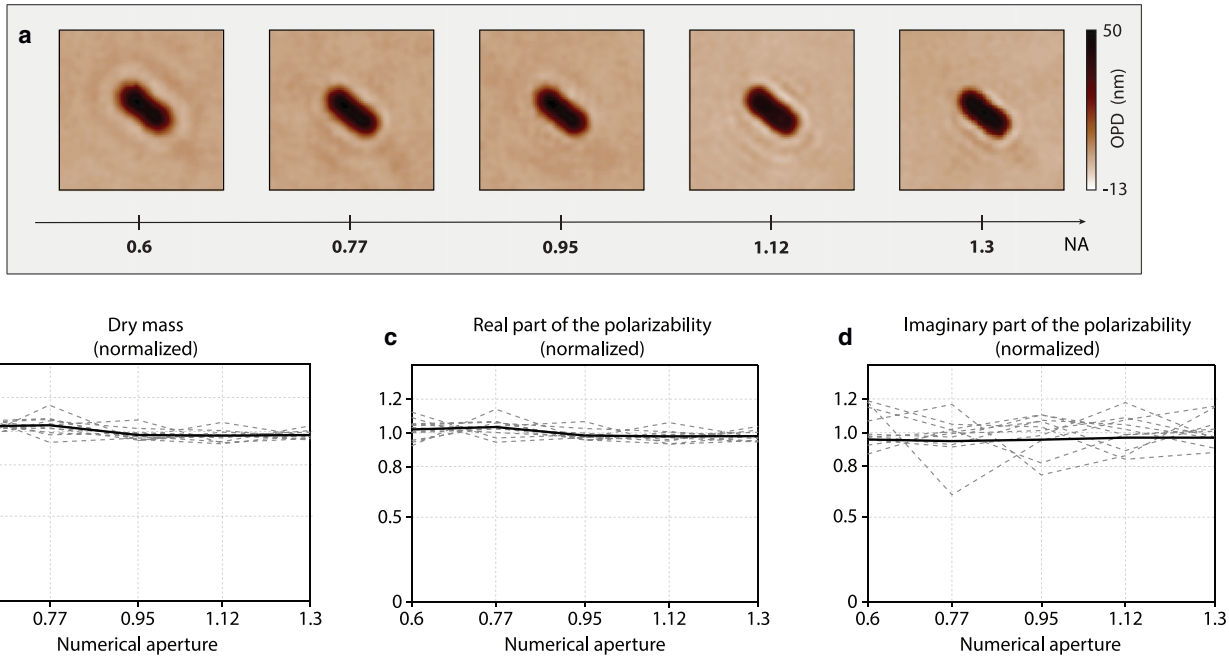

FIGURE 8 Dependence of DM and OP on the objective numerical aperture. (*a*) OPD images of a single bacterium for different objective numerical apertures (100×, 0.6–1.3 NA, $\lambda = 540$ nm). (*b*) Normalized DM as a function of the NA for 10 different bacteria (*dashed lines*), along with the average of all these line shapes (*solid line*). (*c*) Same as (*b*) for Re(α). (*d*) Same as (*c*) for Im(α). To see this figure in color, go online.

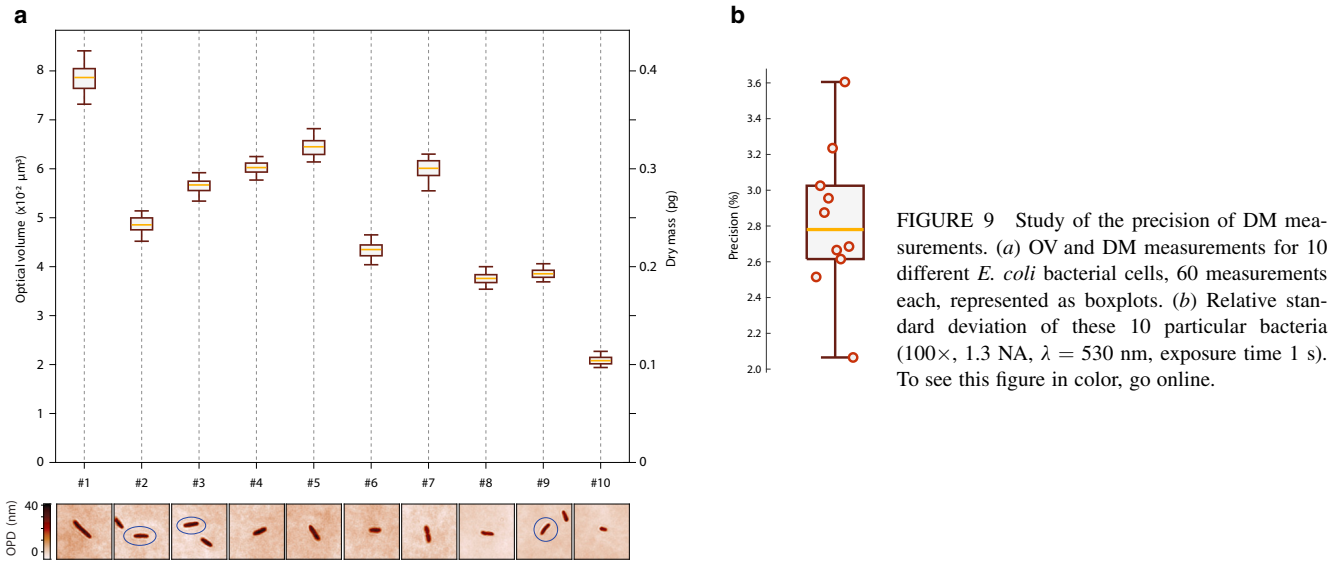

FIGURE 9 Study of the precision of DM measurements. (*a*) OV and DM measurements for 10 different *E. coli* bacterial cells, 60 measurements each, represented as boxplots. (*b*) Relative standard deviation of these 10 particular bacteria (100×, 1.3 NA, $\lambda = 530$ nm, exposure time 1 s). To see this figure in color, go online.

average), and the measured noise amplitude on the images was 0.72 nm (measured on an empty field of view, 431× 450 pixels). This noise level is common in CGM, and can be improved by averaging more OPD images. These 600 OV measurements are presented in Fig. 9. For each bacterium, boxplots are displayed, giving the average OV along with the standard deviation. The precision, defined as the standard deviation divided by the OV, calculated over the 600 bacteria measurements, is close to 3% (Fig. 9).

Concept of microscale CFUs

DM metrology using QPM represents a powerful tool to quantitatively measure the growth rate of cells in culture. Their successive replications of prokaryotic cells can yield the formation of groups of cells in close vicinity (clusters or chains, see Fig. 10), making segmentation and DM estimations of single cells complicated. Nevertheless, to properly estimate the growth rate of a bacteria/archaea population using QPM, it makes sense to follow the mass of a group of cells originating from a single one. On the contrary, such a cell agglomeration is thus not problematic. We call it a microscale CFU (mCFU), in reference to the CFUs that are visually observed in petri dishes at the macroscale (46).

Examples of applications

Monitoring of the growth rate of bacteria over time

As an illustration of the methods and concepts introduced in the previous section, related to DM measurements using CGM, we present here results related to the growth of *E. coli* over time followed by CGM. We followed in real time the bacteria proliferation and quantified the growth rate by monitoring the DMs of several mCFUs over time. The bacteria were incubated at their optimum growth temperature of 37°C. The bacterial cells were imaged using a 40× air objective, at $\lambda = 625$ nm. An image sequence was acquired for >5 h to capture the growth of several mCFUs originating from single bacteria. Fig. 11 plots the average of the DM evolution for five different mCFUs in both normal scale (Fig. 11 *a*) and semilogarithmic scale (Fig. 11 *b*). An exponential growth is observed, followed by a plateau after 4 h corresponding to the expected stationary phase reached when the bacterial cell density is too high. The data were fitted using an exponential function $m = m_0\, 10^{t/\tau} + \text{cst}$, where $g = 1/\tau$ is the growth rate (number of division per unit time). The growth rate at 37°C was found to be $g = 0.71\ \text{h}^{-1}$, which is consistent with culture conditions used in this study.

In all these measurements on mCFUs, we used the same procedure as the one described for single bacteria, involving a dilation factor and a plateau (Fig. 5).

We take the opportunity here to show how CGM, coupled with a fast microheating system (VAHEAT, Interherence), can be conveniently used to investigate the effect of the temperature on the growth rate of microorganisms. Fig. 11 presents results on the growth of *E. coli* at two temperatures, namely 31 and 37°C. The DM evolution of mCFUs is presented in a semilog scale in Fig. 11 *c* to better demonstrate the exponential growth, corresponding here to a linear trend. In both cases, the DM exponentially increases over time before reaching a stationary phase for both temperatures. Faster bacterial growth is observed at 37°C compared with 31°C, as expected, and this variation could be quantitatively estimated; 0.71 h^{-1} at 37°C and 0.34 h^{-1} at 31°C. This is

Please cite this article in press as: Bénéfice et al., Dry mass photometry of single bacteria using quantitative wavefront microscopy, Biophysical Journal (2023), https://doi.org/10.1016/j.bpj.2023.06.020

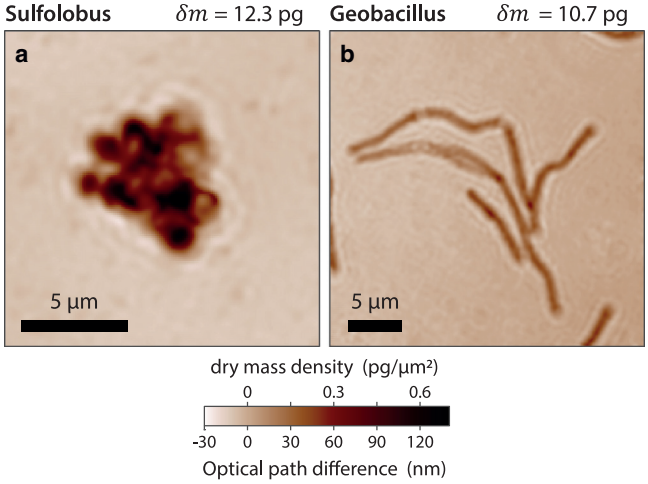

FIGURE 10 Examples of microscale colony-forming units (mCFUs). (*a*) mCFU of *Sulfolobus shibatae* archaea. (*b*) mCFU of *Geobacillus stearothermophilus* bacteria. The measured DMs of the mCFUs are indicated on top of the images (60×, 1.25 NA, $\lambda = 625$ nm). To see this figure in color, go online.

in agreement with previously reported values from the literature (47). The bacterial growth rate slowly increases until its optimum temperature of 37°C then drops for temperatures higher than 37°C.

Toward the differentiation of bacteria using α measurements

The complex OP α of a particle is of utmost interest when the particle is used for its optical properties: α contains all the information related to its interaction with light (e.g., scattering and absorption properties). CGM appears thus as a precious metrology tool in nanophotonics. However, for bacteria, the interest of α is not as straightforward, because one is not particularly interested in their optical properties. Here, we show to what extent α measurements can represent nevertheless an interesting approach in biology, to enrich phase or wavefront images of bacteria.

The specificity of the OP is that it combines not only two images (intensity and OPD), but also two numbers: its real and imaginary parts. Just like the DM, these two numbers scale as the cell volume. Thus, by taking their ratio, the argument of α, or any other such combination, one ends up with a dimensionless quantity that no longer depends on the volume of the bacteria, but on its nature. Combining intensity and phase images to obtain α enables thus the derivation of ratiometric measurements, and possibly to a new method to discriminate different prokaryotic species with similar phenotypes. We investigated this possibility by screening experiments on four different bacteria species, namely *E. coli, G. stearothermophilus, D. radiodurans*, and *L. reuteri*. Results are gathered in Fig. 12. We chose to plot the argument of complex polarizability $\arg(\alpha)$ as a ratiometric, volume-independent quantity. The results show that different species can exhibit different average α

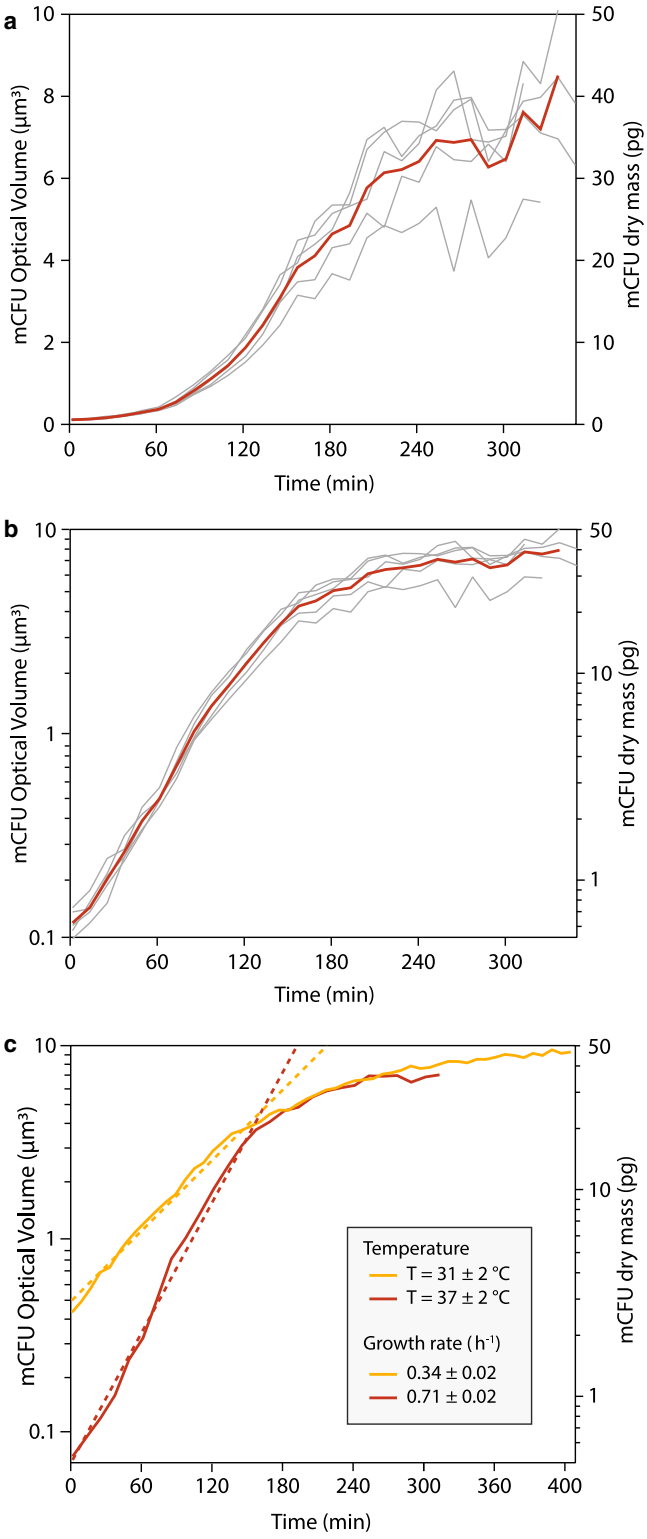

FIGURE 11 (*a*) DM evolution of five *E. coli* mCFUs cultured at 37°C along with the averaged plot. (*b*) Same data as (*a*) in a semilog scale. (*c*) DM evolution of two *E. coli* mCFUs cultured at 31 and 37°C. 40× air objective, $\lambda = 625$ nm. To see this figure in color, go online.

Please cite this article in press as: Bénéfice et al., Dry mass photometry of single bacteria using quantitative wavefront microscopy, Biophysical Journal (2023), https://doi.org/10.1016/j.bpj.2023.06.020

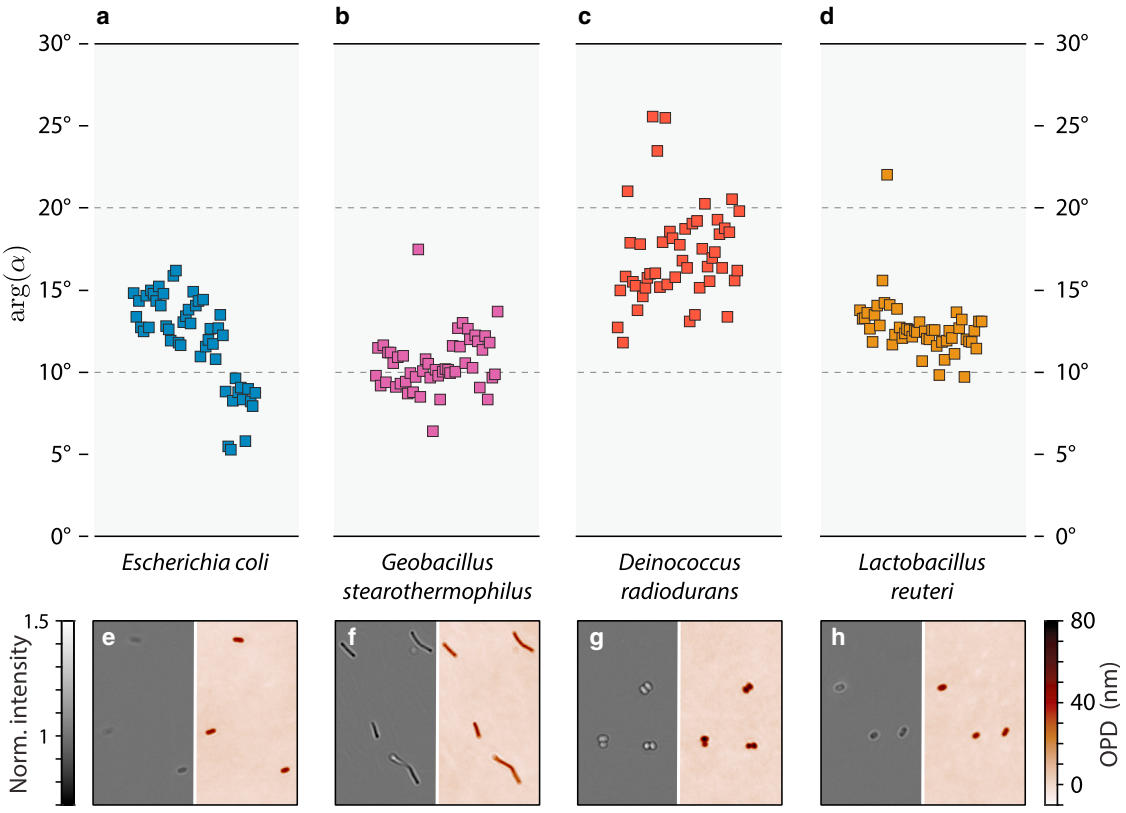

FIGURE 12 Complex OP measurements using CGM for various types of bacteria, namely (*a*) *Escherichia coli*, (*b*) *Geobacillus stearothermophilus*, (*c*) *Deinococcus radiodurans*, and (*d*) *Lactobacillus reuteri*. (*e–h*) Examples of OPD images associated with these four bacteria species. To see this figure in color, go online.

values. $\arg(\alpha)$ appears as a balance between absorption and refraction. What would make $\arg(\alpha)$ (or any other ratiometric quantity) different from one bacterial species from another is thus different ratios of absorption coefficient and refractive indices. More sophisticated ratiometric quantities could be designed to possibly make the measurements less dispersed and make this method more efficient for a better identification.

The results presented in Fig. 12 are not convincing enough to be used to differentiate microorganisms: the data look dispersed and the difference in $\arg(\alpha)$ from one species to another is not blatant. However, there is a difference, and the results presented here highlight a more general concept: the interest of considering also the intensity image, and not only the OPD image, to gain information on the imaged cells. For instance, the group of Park and co-workers recently developed a deep learning approach to identify bacterial species, but just from phase images not on intensity ones (33). Our results suggest here that feeding the artificial neural network (ANN) with not only phase or OPD images but also with the corresponding intensity images could markedly improve the ability of ANN to classify objects imaged with phase and wavefront microscopy techniques. Results presented in Fig. 12 could be more convincing by investigating more complex ratiometric measurements than simply $\arg(\alpha)$, but also by letting an ANN find its optimized combination.

CONCLUSION

DM photometry of bacteria using phase or wavefront microscopy demands a careful control of diffraction, image noise, and focus to achieve accurate measurements. We provide numerical tools and experimental rules to achieve accurate DM measurements of microorganisms, and illustrate these approaches by measurements obtained using CGM.

In addition to the well-known DM, and the OV from which it is derived, we introduce two other physical quantities that expand the toolbox for microorganism characterization using quantitative phase and wavefront microscopies: weighted OV and complex OP. Weighted OV, computed from the OPD image normalized by the square root of the intensity image, gives rise to OV and DM measurements that are no longer dependent on the focus, leading to more precise measurements. Complex OP was introduced a few years ago in the context of nanophotonics to derive their optical properties. We show here that useful quantities can be derived from the OP, such as the argument of OP supposed to be size independent and only dependent on the nature of the microorganism.

Please cite this article in press as: Bénéfice et al., Dry mass photometry of single bacteria using quantitative wavefront microscopy, Biophysical Journal (2023), https://doi.org/10.1016/j.bpj.2023.06.020

This article aims to pave the way for more accurate DM measurement of small biological objects such as microorganisms, organelles, vesicles, or virions, and expands the functionalities of phase/wavefront microscopy to capture original features that can help in the development of refined deep learning algorithms aimed at classifying bacteria.

Although demonstrated using CGM, the results and techniques described in this article can be applied to any QPI.

AUTHOR CONTRIBUTIONS

G.B. conceived the project. M.B. prepared the samples, conducted the experiments, and analyzed the data. A.G., V.D.C., and P.F. trained M.B. for the culture of microorganisms and provided their expertise in microbiology all along the project. B.M. developed and adapted the program to pilot the experimental setup and assisted M.B. in conducting the experiments. G.B. ran the simulations using IF-DDA in close collaboration with P.C.C. and A.S., who developed this code. M.B. and G.B. wrote the manuscript with input from all authors.

ACKNOWLEDGMENTS

This project received funding from the European Research Council under the European Union's Horizon 2020 Research and Innovation Program (grant agreement no. 772725, project HiPhore).

DECLARATION OF INTERESTS

The authors declare no competing interests.

REFERENCES

1. Barr, E. S. 1955. Concerning index of refraction and density. *Am. J. Phys.* 23:623–624.
2. Barer, R. 1957. Refractometry and interferometry of living cells. *J. Opt. Soc. Am.* 47:545–556.
3. Gul, B., S. Ashraf, …, I. Ahmad. 2021. Cell refractive index: Models, insights, applications and future perspectives. *Photodiagnosis Photodyn. Ther.* 33, 102096.
4. Khan, R., B. Gul, …, I. Ahmad. 2021. Refractive index of biological tissues: Review, measurement techniques, and applications. *Photodiagnosis Photodyn. Ther.* 33, 102192.
5. Wientzeck, C., H. Bröhl, and J. Bereiterhahn. 1979. Determination of cellular dry mass by automatic micro-interferometry. *Microsc. Acta.* 3:155–160.
6. Zicha, D., and G. A. Dunn. 1995. An image processing system for cell behaviour studies in subconfluent cultures. *J. Microsc.* 179:11–21.
7. Popescu, G., Y. Park, …, K. Badizadegan. 2008. Optical imaging of cell mass and growth dynamics. *Am. J. Physiol. Cell Physiol.* 295:C538–C544.
8. Rappaz, B., E. Cano, …, P. Marquet. 2009. Noninvasive characterization of the fission yeast cell cycle by monitoring dry mass with digital holographic microscopy. *J. Biomed. Opt.* 14, 034049.
9. Mir, M., Z. Wang, …, G. Popescu. 2011. Optical measurement of cycle-dependent cell growth. *Proc. Natl. Acad. Sci. USA.* 108:13124–13129.
10. Girshovitz, P., and N. T. Shaked. 2012. Generalized cell morphological parameters based on interferometric phase microscopy and their application to cell life cycle characterization. *Biomed. Opt. Express.* 3:1757–1773.
11. Baffou, G. 2023. Wavefront microscopy using quadriwave lateral shearing interferometry: from bioimaging to nanophotonics. *ACS Photonics.* 10:322–339.
12. Primot, J., and N. Guerineau. 2000. Achromatic Optical Interferometer with Continuously Adjustable Sensitivity. https://patents.google.com/patent/US6577403B1/en.
13. Baffou, G. 2021. Quantitative phase microscopy using quadriwave lateral shearing interferometry (QLSI): principle, terminology, algorithm and grating shadow description. *J. Phys. D Appl. Phys.* 54, 294002.
14. Marthy, B., and G. Baffou. 2022. Cross-grating phase microscopy (CGM): In silico experiment (insilex) algorithm, noise and accuracy. *Opt. Commun.* 521, 128577.
15. Aknoun, S., J. Savatier, …, S. Monneret. 2015. Living cell dry mass measurement using quantitative phase imaging with quadriwave lateral shearing interferometry: an accuracy and sensitivity discussion. *J. Biomed. Opt.* 20, 126009.
16. Sridharan, S., M. Mir, and G. Popescu. 2011. Simultaneous optical measurements of cell motility and growth. *Biomed. Opt. Express.* 2:2815–2820.
17. Phillips, K. G., S. L. Jacques, and O. J. T. McCarty. 2012. Measurement of single cell refractive index, dry mass, volume, and density using a transillumination microscope. *Phys. Rev. Lett.* 109, 118105.
18. Cooper, K. L., S. Oh, …, C. J. Tabin. 2013. Multiple phases of chondrocyte enlargement underlie differences in skeletal proportions. *Nature.* 495:375–378.
19. Sung, Y., A. Tzur, …, M. W. Kirschner. 2013. Size homeostasis in adherent cells studied by synthetic phase microscopy. *Proc. Natl. Acad. Sci. USA.* 110:16687–16692.
20. Zangle, T. A., and M. A. Teitell. 2014. Live-cell mass profiling: an emerging approach in quantitative biophysics. *Nat. Methods.* 11:1221–1228.
21. Cintora, P., J. Arikkath, …, C. Best-Popescu. 2017. Cell density modulates intracellular mass transport in neural networks. *Cytometry A.* 91:503–509.
22. Park, H. S., S. Ceballos, …, A. Wax. 2018. Invited article: Digital refocusing in quantitative phase imaging for flowing red blood cells. *APL Photonics.* 3, 110802.
23. Tolde, O., A. Gandalovičová, …, J. Brábek. 2018. Quantitative phase imaging unravels new insight into dynamics of mesenchymal and amoeboid cancer cell invasion. *Sci. Rep.* 8, 12020.
24. Kandel, M. E., W. Lu, …, G. Popescu. 2019. Cell-to-cell influence on growth in large populations. *Biomed. Opt. Express.* 10:4664–4675.
25. Midtvedt, D., E. Olsén, …, G. D. M. Jeffries. 2019. Label-free spatiotemporal monitoring of cytosolic mass, osmolarity, and volume in living cells. *Nat. Commun.* 10:340.
26. Sandoz, P. A., C. Tremblay, …, M. Frechin. 2019. Image-based analysis of living mammalian cells using label-free 3D refractive index maps reveals new organelle dynamics and dry mass flux. *PLoS Biol.* 17, e3000553.
27. Ayyappan, V., A. Chang, …, R. Pandey. 2020. Identification and staging of B-cell acute lymphoblastic leukemia using quantitative phase imaging and machine learning. *ACS Sens.* 5:3281–3289.
28. Aknoun, S., M. Yonnet, …, P. Pognonec. 2021. Quantitative phase microscopy for non-invasive live cell population monitoring. *Sci. Rep.* 11:4409.
29. Park, K., J. Jang, …, R. Bashir. 2008. 'Living cantilever arrays' for characterization of mass of single live cells in fluids. *Lab Chip.* 8:1034–1041.
30. Bryan, A. K., A. Goranov, …, S. R. Manalis. 2010. Measurement of mass, density, and volume during the cell cycle of yeast. *Proc. Natl. Acad. Sci. USA.* 107:999–1004.
31. Godin, M., F. F. Delgado, …, S. R. Manalis. 2010. Using buoyant mass to measure the growth of single cells. *Nat. Methods.* 7:387–390.
32. Park, K., L. J. Millet, …, R. Bashir. 2010. Measurement of adherent cell mass and growth. *Proc. Natl. Acad. Sci. USA.* 107:20691–20696.

33. Kim, G., D. Ahn, …, Y. Park. 2022. Rapid species identification of pathogenic bacteria from a minute quantity exploiting three-dimensional quantitative phase imaging and artificial neural network. *Light Sci. Appl.* 11:190.

34. Shin, J., G. Kim, …, Y. Park. 2023. Long-term label-free assessments of individual bacteria using three-dimensional quantitative phase imaging and hydrogel-based immobilization. *Sci. Rep.* 13:46.

35. Primot, J., and N. Guérineau. 2000. Extended Hartmann test based on the pseudoguiding property of a Hartmann mask completed by a phase chessboard. *Appl. Opt.* 39:5715–5720.

36. Bon, P., G. Maucort, …, S. Monneret. 2009. Quadriwave lateral shearing interferometry for quantitative phase microscopy of living cells. *Opt. Express.* 17:13080–13094.

37. Khadir, S., P. Bon, …, G. Baffou. 2017. Optical imaging and characterization of graphene and other 2D materials using quantitative phase microscopy. *ACS Photonics.* 4:3130–3139.

38. Khadir, S., P. C. Chaumet, …, A. Sentenac. 2019. Quantitative model of the image of a radiating dipole through a microscope. *J. Opt. Soc. Am. A.* 36:478–484.

39. Khadir, S., D. Andrén, …, G. Baffou. 2020. Full optical characterization of single nanoparticles using quantitative phase imaging. *Optica.* 7:243.

40. Khadir, S., D. Andrén, …, G. Baffou. 2021. Metasurface optical characterization using quadriwave lateral shearing interferometry. *ACS Photonics.* 8:603–613.

41. Chaumet, P. C., D. Sentenac, …, A. Sentenac. 2021. IFDDA, an easy-to-use code for simulating the field scattered by 3D inhomogeneous objects in a stratified medium: Tutorial. *J. Opt. Soc. Am. A.* 38:1841.

42. Chaumet, P. C. 2022. The discrete dipole approximation: A review. *Mathematics.* 10:3049.

43. Durdevic, L., A. Relaño Ginés, …, G. Baffou. 2022. Biomass measurements of single neurites in vitro using optical wavefront microscopy. *Biomed. Opt. Express.* 13:6550–6560.

44. Bénéfice, M., and G. Baffou. 2022. Github repository: Segmentation tool for wavefront microscopy. github.com/baffou/CGM_magicWandSegmentation.

45. Young, G., N. Hundt, …, P. Kukura. 2018. Quantitative mass imaging of single molecules. *Science.* 360:423–427.

46. Molinaro, C., M. Bénéfice, …, G. Baffou. 2022. Life at high temperature observed in vitro upon laser heating of gold nanoparticles. *Nat. Commun.* 13:5342.

47. Noor, R., Z. Islam, …, F. Rahman. 2013. Influence of temperature on *Escherichia coli* growth in different culture media. *J. Pure Appl. Microbiol.* 7:899–904.